Physics Faculty Research & Creative Works

Physics

12 Apr 2022

Fluoride Doping in Crystalline and Amorphous Indium Oxide Semiconductors

Aritra Sil

Michael J. Deck

Elise A. Goldfine

Chi Zhang

et. al. For a complete list of authors, see *https://scholarsmine.mst.edu/phys_facwork/2247*

Recommended Citation

A. Sil and M. J. Deck and E. A. Goldfine and C. Zhang and S. V. Patel and S. Flynn and H. Liu and P. H. Chien and K. R. Poeppelmeier and V. P. Dravid and M. J. Bedzyk and J. E. Medvedeva and Y. Y. Hu and A. Facchetti, "Fluoride Doping in Crystalline and Amorphous Indium Oxide Semiconductors," *Chemistry of Materials*, vol. 34, no. 7, pp. 3253 - 3266, American Chemical Society, Apr 2022.
The definitive version is available at https://doi.org/10.1021/acs.chemmater.2c00053

Fluoride Doping in Crystalline and Amorphous Indium Oxide Semiconductors

Aritra Sil,[¶] Michael J. Deck,[¶] Elise A. Goldfine, Chi Zhang, Sawankumar V. Patel, Steven Flynn, Haoyu Liu, Po-Hsiu Chien, Kenneth R. Poeppelmeier,* Vinayak P. Dravid,* Michael J. Bedzyk,* Julia E. Medvedeva,* Yan-Yan Hu,* Antonio Facchetti,* and Tobin J. Marks*

Read Online

ACCESS | Metrics & More | Article Recommendations | SI Supporting Information

ABSTRACT: In this contribution, the structural and electronic effects of fluoride doping in both crystalline and amorphous indium oxides are investigated by both experimental and theoretical techniques. Pristine crystalline and amorphous fluoride-doped indium oxide (F:In−O) phases were prepared by solution-based combustion synthesis and sol−gel techniques, respectively. The chemical composition, environment, and solid-state microstructure of these materials were extensively studied with a wide array of state-of-the-art techniques such as UV−vis, X-ray photoelectron spectroscopy, grazing incidence X-ray diffraction, ^{19}F and ^{115}In solid-state NMR, high-resolution transmission electron microscopy (HR-TEM), and extended X-ray absorption fine structure (EXAFS) as well as by density functional theory (DFT) computation combined with MD simulations. Interestingly, the UV−vis data reveal that while the band gap increases upon F⁻-doping in the crystalline phase, it decreases in the amorphous phase. The ^{19}F solid-state NMR data indicate that upon fluorination, the InO_3F_3 environment predominates in the crystalline oxide phase, whereas the InO_4F_2 environment is predominant in the amorphous oxide phase. The HR-TEM data indicate that fluoride doping inhibits crystallization in both crystalline and amorphous In−O phases, a result supported by the ^{115}In solid-state NMR, EXAFS, and DFT-MD simulation data. Thus, this study establishes fluoride as a versatile anionic agent to induce disorder in both crystalline and amorphous indium oxide matrices, while modifying the electronic properties of both, but in dissimilar ways.
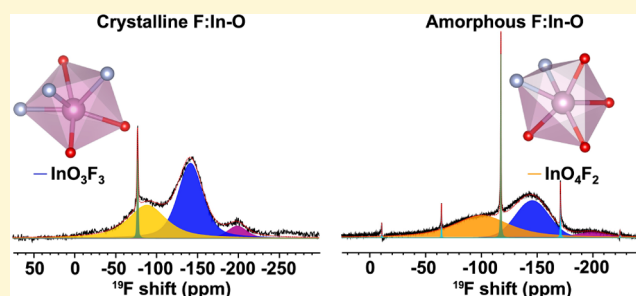
■ INTRODUCTION

In recent years, solution-processed metal-oxide (MO)-based semiconductors have brought about a revolution in the field of high-resolution, transparent, and flexible display technologies because of their superior charge transport properties (carrier mobility, $\mu \sim 1–100$ cm^2 V^{-1} s^{-1}) in the amorphous state, excellent visible light transparency (>85%), as well as proven mechanical flexibility.[1−9] Compared to conventional widely used low-temperature polycrystalline silicon technologies, amorphous MOs (a-MOs) offer unique advantages, particularly in fabrication by solution processing using inexpensive and air-stable inorganic salt precursors.[10−12] Furthermore, a-MOs can overcome the low electron mobility ($\mu \sim 0.5–1.0$ cm^2 V^{-1} s^{-1}) and poor optical transparency of amorphous silicon, the current semiconductor of choice in most displays.[13,14] Compared to other next-generation unconventional semiconductors such as organic and 2D (e.g., graphene, MoS_2, etc.) materials, a-MO semiconductors exhibit superior scalability, chemical stability, amenability to integration, and excellent optical transparency,[15−19] thereby finding applications ranging from solar cell interfacial layers to gas sensors and bioelectronics.[20−23]

Much of the technological success of a-MO semiconductors in thin-film transistor (TFT) applications originates from the high electron mobility in the amorphous state. Because performance uniformity over large areas in TFT panels is generally inversely related to the crystallinity of the metal oxide matrices, there have been extensive efforts to tune charge transport−microstructure properties primarily through doping with cations functioning both as "oxygen getters" and enhancers of the crystallization temperature. In the case of In-based MOs, these cations have stronger M−O bonding than In−O (e.g., Ga^{3+}, Sc^{3+}, Y^{3+}, and Zn^{2+}).[5,24−28] For example, in a pioneering study, Moffitt et al. showed that in In−Ga−O, Ga prefers the local oxygen environment of pure Ga_2O_3 to that of the In−O matrix owing to stronger Ga−O versus In−O bonding, therefore increasing the crystallization temperature of
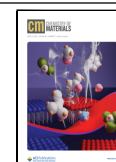
In−Ga−O, hence the amorphous character of this oxide material.[29] Alternatively, this Laboratory discovered that insulating polymers such as polyethyleneimine (PEI) and poly(vinyl phenol) (PVP) can be used to reduce the crystallinity, control the carrier concentration, and tune the work function of metal oxide matrices.[30−33] For example, the addition of PVP to In_2O_3 matrices inhibits its crystallization and reduces its mobility; however, PEI also amorphizes the matrix but also increases the mobility for optimal PEI contents.[31−33] We also recently discovered that the addition of poly(vinyl alcohol) in IGO enhances mobility by ∼70 times via hydrogen doping. The process creates a Ga···H distance of ∼3.4 Å and conversion from six- to four-coordinate Ga, which also suppresses deep trap defect localization.[30] Building further on these results, a two-dimensional electron gas based on high-performance oxide homojunction TFTs has also been realized.[34]

With the goal of further enhancing MO semiconductor opto-electronics properties, anion-doping of other metal oxides has recently been explored, albeit to a much lesser degree.[35−37] Taking advantage of the variable electronegativities, band gaps, and microstructures that groups 15, 16, and 17 elements can potentially impart, their anion-doping may provide unusual and instructive opto-electronic performance modifications. Fluoride (F−) is an especially suitable anion to dope MOs due to a similar ionic radius to an oxide dianion ($F^{1−}$: 1.285 Å, $O^{2−}$: 1.35 Å).[38] Indeed, upon fluoride-doping of MOs by both physical vapor deposition (PVD, e.g., sputtering and pulsed-laser deposition)[39−43] and sol−gel techniques,[44−46] the carrier mobility of MO-based TFTs (e.g., In−Ga−Zn−O, ZnO, and Zn−Sn−O) is found to increase by ∼30−40%.[39−43] However, PVD-based techniques are capital-intensive and incompatible with next-generation roll-to-roll fabrication techniques, and anionic precursors can be very corrosive to vacuum systems.[12] Also, sol−gel processes typically require long annealing times and high temperatures.[44−46] Importantly, unlike the cation-doping of metal oxides, structure−function relationships have not been widely explored in anion-doped systems,[39−46] which hinders further development of these materials. Thus, it is important to explore new anion-doped MOs, and to find new ways to produce them, for a better understanding of how properties are affected as well as routes to implement them in unconventional optoelectronics.

Recently, this Laboratory investigated the effect of fluoride-doping on structure−function relationships in amorphous indium oxide matrices.[47] Charge transport properties measured in TFTs reveal that as the F− content in F:In−O increases, both I_{off} and I_{on} fall, while I_{on}/I_{off} increases, thus affording superior TFT switching properties versus undoped In−O-based TFTs. Also, in contrast to previous literature reports,[39−46,48] F−-doping generally reduces the electron mobility in MO matrices.[47] Furthermore, extended X-ray absorption fine structure (EXAFS) analysis revealed that F−-doping disrupts crystallization by enhancing the local and medium-range disorder. The aforementioned charge transport and structural properties of these films were in excellent agreement with ab initio MD simulations and density functional theory (DFT) calculations. Thus, F−-doping increases atomic mobility and enhances deep trap state localization, rationalizing the depression in I_{off} and electron mobility. This was the first in-depth study accurately describing structure−function relationships in a technologically relevant *amorphous* F−-doped oxide semiconductor. Intrigued by these

interesting results and their implications in display technologies, further investigation was warranted to probe the chemical nature of the fluoride anions as well as their role in the microstructure of amorphous versus crystalline indium oxides. The key questions here are whether fluoride anion can also introduce disorder in crystalline oxide matrices similar to that in amorphous oxide matrices and how the chemical environment of fluoride in amorphous oxides compares to that of the analogous crystalline oxides. Ultimately, these questions directly concern the opto-electronic properties of the corresponding amorphous versus crystalline materials, serving as ideal platforms for theoretical analysis to guide future materials design.

Therefore, in this contribution, we compare and contrast the effects of F−-doping in both amorphous and crystalline In−O. The synthetic procedures are optimized to yield fluoride-doped In−O (F:In−O) powders with F− incorporation ranging from 0.0 to 9.2 at. % (at. % vs In 3d) in crystalline oxides and 0.0−19.4 at. % (at. % vs In 3 d) in amorphous oxides. Grazing incidence X-ray diffraction (GIXRD) and X-ray photoelectron spectroscopy (XPS) were used to probe crystallinity and the chemical composition of F:In−O, respectively. [19]F magic-angle spinning (MAS) NMR probed the fluoride local chemical environments in crystalline versus amorphous F:In−O samples—the InO_3F_3 environment is found to predominate in the crystalline oxide phase, and the InO_4F_2 environment predominates in the amorphous oxide phases. In addition, [115]In solid-state NMR probed the effects of fluorination on the indium local environment and the degree of order in the crystalline and amorphous In−O matrices. Finally, the experimental trends are examined in the light of ab initio molecular dynamic (MD) simulations, revealing that F−-doping inhibits crystallization by enhancing the local and medium-range disorder, which in turn is confirmed by EXAFS. High-resolution transmission electron microscopy (HR-TEM) and selected area electron diffraction (SAED) furthermore show that F−-doping decreases grain size in amorphous oxide and weakens diffraction patterns in the crystalline oxides. UV−vis data indicate that while the F−-doping in crystalline In−O increases the band gap, the opposite trend occurs in the amorphous phase, in excellent agreement with DFT calculations. Thus, the close agreement achieved between the theory and experiment provides convincing insights into how F−-doping differently affects structure−property relationships in crystalline versus amorphous indium oxides.

■ RESULTS AND DISCUSSION

Synthesis of Crystalline and Amorphous Fluoride-Doped Indium Oxide. For this study, we investigated the archetypal MO system In−O because it is widely investigated for TFT applications and one of the compositionally simplest MO semiconductors.[11,49−54] Furthermore, any effect of fluoride-doping can be more easily tracked in this system via both theoretical and experimental analyses.[47] The goal is to synthesize pure amorphous and crystalline F:In−O samples in sufficient quantities (∼200 mg) to carry out thorough experiments. Thus, multiple MO synthesis procedures for both crystalline and amorphous samples were explored and optimized (see a summary in Table S1), which includes preparation of precursor solutions of an indium salt, a fluoride source, and optionally, additional components in a solvent (vide infra) followed by deposition of the solution by methods such as spin-coating or drop-casting. Drop-casting was deemed

more suitable for this purpose because highly pure F:In−O samples can be prepared in larger quantities (Figure S1).

F:In−O Synthesis. For the synthesis of crystalline F:In−O (c-F:In−O), combustion synthesis was employed, a technique where a redox (oxidizer + fuel) reagent pair generates appreciable heat to decompose the reactants and form dense MO.[54] Here, indium nitrate $[In(NO_3)_3]$ was used as the indium and oxidizer (NO_3^-) sources, acetylacetone (AcAcH) as the fuel, ammonium hydroxide (NH_4OH) as a base, and 2-methoxyethanol as the solvent. Ammonium fluoride (NH_4F) was used as the fluoride source as it has been previously used to introduce fluoride in the In−O system.[47] The precursor solution was drop-cast on Si wafers and heated at a desired annealing temperature and time on a hot plate to obtain drop-cast MO films (Figure S1). The powder is then obtained by scraping off the film with a razor blade. First, annealing time and temperature were optimized to minimize the amount of carbon and nitrogen impurities (Table S2). The atomic composition (e.g., C and N impurities and fluoride content) was quantified by XPS. Note that even at a low temperature and for short annealing times (120 °C/1 min + 250 °C/1 min), crystalline F:In−O was obtained, although significant N impurities were detected (N:In ∼ 3.3 at. %) (Table S2). As the annealing time and temperature were increased (120 °C/1 min + 330 °C/5 min), relatively pure crystalline F:In−O samples were obtained (C:In ∼ 3.2−4.8 at. % and N:In ∼ 0 at. %) (Figure S2 and Table S2). Next, varying amounts of NH_4F (0−50 at. %) were added to the precursor solution to prepare 0−9.2 at. % doped F:In−O samples. As shown in Table 1, the

Table 1. Fluoride Incorporation in Crystalline and Amorphous In−O Samples

NH_4F soln. concentration[a]	F:In (in soln.) [at. %][b]	F:In (crystalline oxide) [at. %][c]	F:In (amorphous oxide) [at. %][c]
0.00 M NH_4F soln.	N/A	0	0
0.025 M NH_4F soln.	5	2.9	2.5
0.075 M NH_4F soln.	15	5.7	7.2
0.15 M NH_4F soln.	30	7.3	11.9
0.25 M NH_4F soln.	50	9.2	19.4

[a]Precursor solution: conventional In−O precursor soln. (2 mL; see Experimental Section for details) + 7 μL of conc. HNO_3 + 200 μL of 0.00/0.005/0.025/0.075/0.15/0.25 M NH_4F solns. [b]As added to solution. [c]F 1s spectra detected via XPS. F:In ratio calculated by integrating F 1s peak versus In 3d (In $3d_{3/2}$ + In $3d_{5/2}$) peak by Avantage software.

F^- content in the In−O matrices increases from 0 to 2.9 to 5.7 to 7.3 to 9.2 at. %, as the F:In in the solution increases from 0 to 5 to 15 to 30 to 50 at. %, respectively. GIXRD data show that all F:In−O compositions as well as In−O powders are highly crystalline (Figure 1a) and have the bixbyite structure of In_2O_3 (Figures 1a and S3). Moreover, the log scale plot of the GIXRD patterns for c-0 and c-9.2 at. % (Figure S4) further confirms that there are no impurity phases formed upon fluoride doping.

To synthesize amorphous F:In−O (a-F:In−O) samples, the sol−gel method was employed because the large internal heat from the combustion process can crystallize In−O at temperatures as low as 200 °C.[54] For sol−gel synthesis,

$In(NO_3)_3$ was dissolved in 2-methoxyethanol and a base (NH_4OH) with NH_4F as the fluoride source. Employing the same procedure as that producing the crystalline phase (vide supra), the amorphous sample was obtained, as shown in Figure S1, upon optimizing the annealing temperature and time to 120 °C/1 min + 250 °C/10 min to reduce C and N contamination (Table S3). Note that above 120 °C/1 min + 275 °C/5 min, the In−O begins to partially crystallize (Figure S5). These relatively pure and amorphous F:In−O samples have C:In ∼ 6−9 at. % and N:In ∼ 1.3−2 at. % (Figures 1b and S6). From Table 1, it can be seen that, as the F:In in the solution increases from 0 to 5 to 15 to 30 to 50 at. %, the F^- content in In−O matrices increases from 0 to 2.5 to 7.2 to 11.9 to 19.4 at. %, respectively.

From XPS measurements (Figure 1c,d), the binding energy of the F 1s is 684.4 ± 0.4 eV for both amorphous and crystalline samples, which is in excellent agreement with our previous report.[47] Note that the F 1s binding energy of the fluoride anion in F:In−O indicates that F^- binds ionically with In (organic fluoride energies lies in the 688−689 eV range)[55] in all samples. Also, In 3d XPS spectra were acquired (Figure S7). Upon fluoride doping, In 3d binding energy shifts from 443.4 eV in c-In−O to 444.0 eV in c-9.2 at. % F:In−O. A similar trend is observed for the amorphous samples: the In 3d binding energy shifts by 0.5 eV from 443.9 eV in a-In−O to 444.4 eV in a-19.4 at. % F:In−O. The In 3d XPS data further support the fact that F binds strongly to the In ion in both crystalline as well as amorphous oxide powders.

^{1}H MAS NMR Spectroscopy. This technique was next applied to ascertain the purity of the present F:In−O compounds (Figures 1e,f and S8). The chemical shift of ^{1}H in NH_4F is δ 7.4 ppm (Figure S8). Figures 1e and S8a show the ^{1}H MAS NMR spectra for the crystalline samples. Note that the ^{1}H spectra of c-F:In−O remain mostly unchanged over the 2.9−9.2 at. % F^--doping range compared to undoped In−O and several distinct ^{1}H resonance peaks, especially at δ 1.34 ppm are observed in all crystalline samples (Table S4). In the case of amorphous F:In−O, a broad peak centered at δ 3.39 ppm is observed in all samples (Figures 1f, S8b and Table S5). Note, ^{1}H solid-state NMR spectra of all samples do not show a resonance at δ 7.4 ppm, meaning that no NH_4F precursor remains after precursor processing, in excellent agreement with XPS results (vide supra).

^{19}F MAS NMR Spectra. Next, to investigate the F environment in detail, ^{19}F MAS NMR spectra were recorded. As shown in Table 2 and Figure S9, the ^{19}F chemical shifts (δ) of the oxide precursors and relevant standard reference compounds were acquired. The ^{19}F signal of NH_4F and InF_3 are found at δ −82.3 ppm and δ −207.88 ppm, respectively, in good agreement with the literature values.[56,57] To the best of our knowledge, we report the ^{19}F MAS spectrum of InOF $(InO_4F_2$ octahedra) for the first time (δ −128.58 ppm). Also, shown in Table 2 and Figure S10 are the In octahedra of the reference compounds from the ICSD database. Note that the ^{19}F chemical shift increases almost linearly with the increasing number of F ions surrounding the In octahedra, from δ −64.14 ppm in InO_5F octahedra (Ba_2InO_3F), to δ −128.58 ppm in InO_4F_2 octahedra (InOF), to δ −207.88 ppm in InF_6 octahedra (InF_3) (Figure S11). This empirical relationship helps to assign unknown ^{19}F peaks in crystalline and amorphous F:MO species.[58]

Figure 2a shows the ^{19}F MAS NMR spectra of c-F:InO. The ^{19}F NMR spectrum of each crystalline sample can be
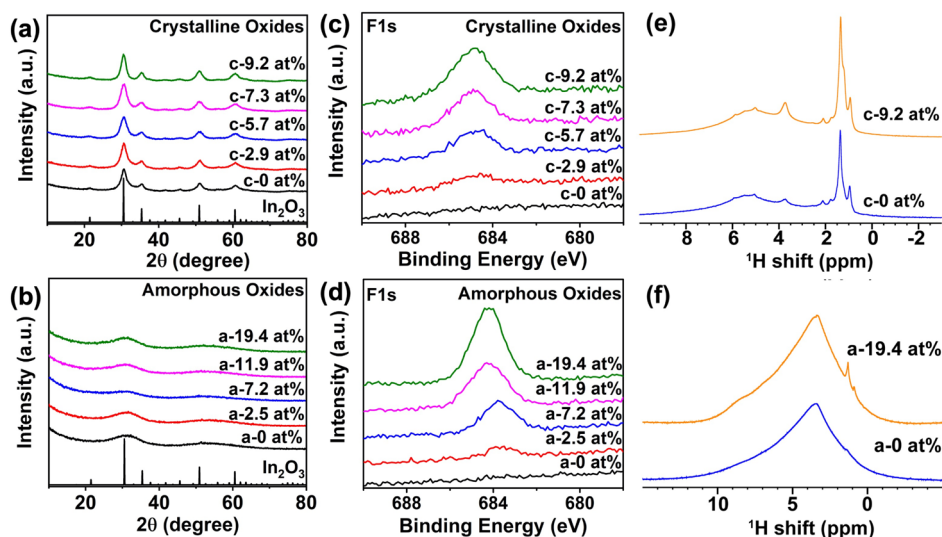
Figure 1. GIXRD patterns of the indicated (a) crystalline x at. % F:In−O and (b) amorphous x at. % F:In−O samples. F1s XPS spectra of the indicated (c) crystalline x at. % F:In−O and (d) amorphous x at. % F:In−O. ^{1}H MAS NMR spectra indicated (e) crystalline x at. % F:In−O and (f) amorphous x at. % F:In−O.

Table 2. ^{19}F MAS NMR Data and Indium Octahedra of the Indicated Compounds

material	^{19}F δ (ppm)	indium octahedra[a]
NH$_4$F	−82.3	N/A
Ba$_2$InO$_3$F	−64.14	InO$_5$F
InOF	−128.58	InO$_4$F$_2$
InF$_3$	−207.88	InF$_6$

[a]Obtained from ICSD database.

deconvoluted into four distinct chemical environments: (1) crystalline-InO$_5$F (δ −78 ppm); (2) InO$_5$F (δ −88 ppm); (3) InO$_3$F$_3$ (δ −142 ppm); and (4) InF$_6$ (δ −199 ppm). Utilizing the chemical shift of reference compounds (Table 2 and Figure S11), the chemical species can be assigned,[58] and the quantitative results are summarized in Table S6 and Figure

S12. A sharp c-InO$_5$F peak is observed at δ −78 ppm, which constitutes about 0.9% for c-2.9 at. % F:In−O, 0.8% for c-5.7 at. % F:In−O, 0.6% for c-7.3 at. % F:In−O, and 2.6% for c-9.2 at. % F:In−O of the total fluoride content. Next, a gradually decreasing peak is observed in the fitting at δ −88 ppm (InO$_5$F) constituting 55.4% for c-2.9 at. % F:In−O, 45.5% for c-5.7 at. % F:In−O, 43.8% for c-7.3 at. % F:In−O, and 37.9% for c-9.2 at. % F:In−O of the total fluoride content. At δ −142 ppm (InO$_3$F$_3$), there is a gradually increasing peak constituting 40.7% for c-2.9 at. % F:In−O, 49.8% for c-5.7 at. % F:In−O, 52.1% for c-7.3 at. % F:In−O, and 52.8% for c-9.2 at. % F:In−O of the total fluoride content. Lastly, at δ −199 ppm (InF$_6$), there is a gradually increasing component composing 2.9% for c-2.9 at. % F:In−O, 4.0% for c-5.7 at. % F:In−O, 3.5% for c-7.3 at. % F:In−O, and 6.7% for c-9.2 at. % F:In−O of the total fluoride content.
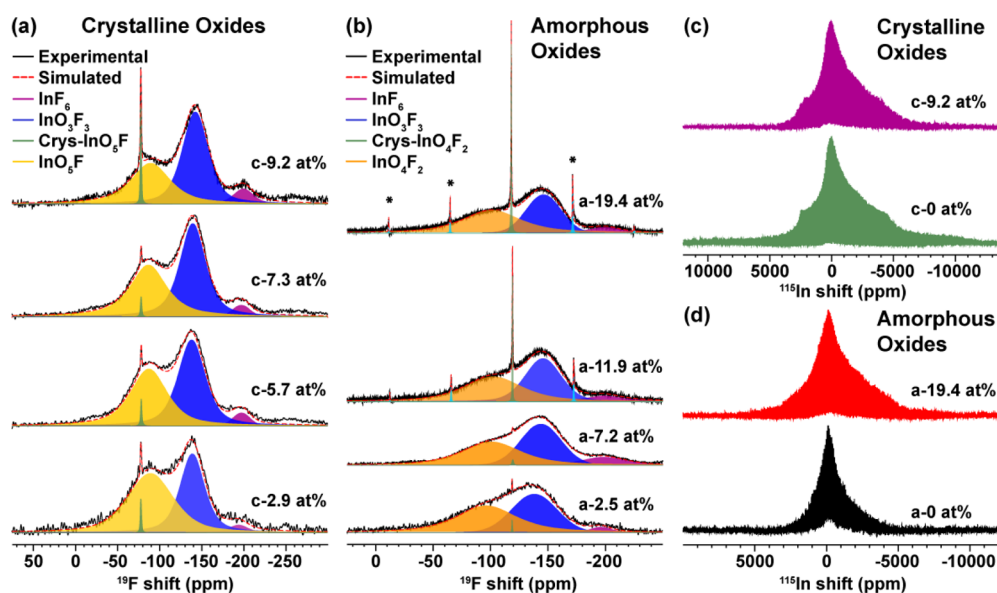

Figure 2. ^{19}F MAS NMR spectra of the indicated (a) crystalline x at. % F:In−O and (b) amorphous x at. % F:In−O. Asterisks represent spinning sidebands. ^{115}In static solid-state NMR spectra of indicated (c) crystalline x at. % F:In−O and (d) amorphous x at. % F:In−O.

Next, ^{19}F MAS NMR spectra of the a-F:In−O samples were acquired and deconvoluted into four major chemical species: (1) InO_4F_2 (δ −102 ppm); (2) crystalline-InO_4F_2 (δ −119 ppm); (3) InO_3F_3 (δ −146 ppm); and (4) InF_6 (δ −199 ppm) (Figure 2b). The broad nature of the ^{19}F peaks signifies that the amorphous samples are more disordered than the crystalline analogues. Following the quantitative analysis (Table S7 and Figure S13), the sharp peak observed at δ −119 ppm (crystalline-InO_4F_2) constitutes 0.3% for a-2.5 at. % F:In−O, 0.3% for a-7.2 at. % F:In−O, 2.9% for a-11.9 at. % F:In−O, and 5.8% for a-19.4 at. % F:In−O. A peak at δ −102 ppm (InO_4F_2) constitutes 52.9% for a-2.5 at. % F:In−O, 45.4% for a-7.2 at. % F:In−O, 45.9% for a-11.9 at. % F:In−O, and 49.7% for a-19.4 at. % F:In−O. InO_3F_3 polyhedra at δ −146 ppm constitute 43.4% for a-2.5 at. % F:In−O, 43.6% for a-7.2 at. % F:In−O, 43.4% for a-11.9 at. % F:In−O, and 38.3% for a-19.4 at. % F:In−O. Lastly, a peak is observed at δ −199 ppm (InF_6), which constitutes 3.5% for a-2.5 at. % F:In−O, 10.7% for a-7.2 at. % F:In−O, 7.8% for a-11.9 at. % F:In−O, and 6.2% for a-19.4 at. % F:In−O. The results show that upon fluorination, octahedral InO_4F_2 is the predominant environment in the amorphous samples, in contrast to octahedral InO_3F_3 in the crystalline samples. The shifts of all octahedra from the ^{19}F NMR measurements are shown in Figure S14.

^{115}In NMR Spectra. ^{115}In static solid-state NMR spectra for both c-F:InO and a-F:InO can be seen in Figure 2c,d. Note that ^{115}In (nuclear spin = 9/2) signal is very broad (linewidths of >1 MHz) due to the large quadrupole moment of ^{115}In (77.0 fm^2).[59,60] This poses fundamental challenges in acquiring wideline spectra for comprehensive analysis using QCPMG alone as the radiofrequency pulses cannot excite the entire spectral range. Therefore, to increase the excitation bandwidth, QCPMG combined with a frequency-stepped method was used to collect individual spectra at evenly spaced transmitter offset-frequency intervals of ±166 kHz (γB_1). The overall ^{115}In NMR spectrum was then obtained by superimposing each individual spectrum.[30,61,62] On comparing the fluorine-free and fluorinated samples, it can be seen that the In local environment becomes more disordered after F$^-$-doping, indicated by the smeared-out edges of the quadrupolar lineshape (Figure 2c) and the significantly broadened spectral linewidth (Figure 2d), which implies an increase in the quadrupolar coupling constant (C_Q), in complete agreement with literature.[30,63−65] This result is consistent with EXAFS, MD simulation, and TEM results (vide infra).

XPS O 1s Analysis. XPS O 1s data were next analyzed to quantify the effect of F$^-$-doping on the MO lattice content of the present samples (Tables S8 and S9, Figures 3 and S15). The O 1s spectra can be deconvoluted into three distinct
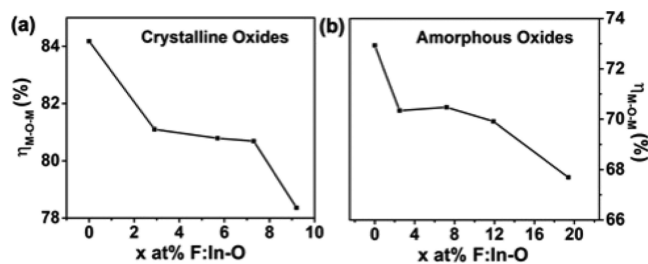
chemical environments: (1) metal oxide lattice (M−O−M) at 529.9 ± 0.1 eV; (2) metal hydroxide (M−OH) species at 531.1 ± 0.1 eV; and (3) weakly bound CO_2 and H_2O, species (M−OR) at 532.2 ± 0.1 eV.[24,66] The metal oxide lattice (M−O−M) is primarily responsible for efficient carrier transport through the MO matrices, whereas M−OR and M−OH act as trap states.[50,67,68] Therefore, the M−O−M lattice content (η_{M-O-M}) defined as the ratio of the M−O−M peak area to the entire O 1s peak area can be utilized as a figure of merit for the quality of the In−O matrices.[24,69] As shown in Table S8 and Figure 3a, high M−O−M (78.4−84.2%) content is observed in the crystalline oxide. This is in accord with literature data, indicating that the exothermic heat of combustion synthesis densifies the M−O−M matrices.[66,70] With the addition of fluoride to the MO matrices, η_{M-O-M} falls gradually to 84.2% for c-In−O, to 81.1% for c-2.9 at. % F:In−O, to 80.8% for c-5.7 at. % F:In−O, to 80.7% for c-7.3 at. % F:In−O, and finally dropping to 78.4% for c-9.2 at. % F:In−O. In the amorphous oxides (Table S9 and Figure 3b), lower content of the M−O−M lattice (67.7−72.9%) compared to crystalline oxides is observed due to the minimal exothermic heat of reaction in the present sol−gel process. With incorporation of fluoride, η_{M-O-M} consistently falls from 72.9% for a-In−O, to 70.3% for a-2.5 at. % F:In−O, 70.5% for a-7.2 at. % F:In−O, 69.9% for a-11.9 at. % F:In−O, and then to 67.7% for a-19.4 at. % F:In−O. Thus, in both crystalline and amorphous oxides, F$^-$-doping slightly decreases M−O−M lattice content, in excellent agreement with literation anticipation.[47]

Optical Absorption Analysis. UV−vis spectra were acquired utilizing diffuse reflectance methods on drop-cast thin films on silicon substrates (Figure S16). Band gap values were extracted utilizing the Kubelka−Munk equation.[71] As shown in Table S10 and Figure 4a, the band gap of the crystalline samples increases linearly from 2.48 eV for c-In−O, to 2.52 eV for 2.9 at. % F:In−O, to 2.55 eV for c-5.7 at. % F:In−O, to 2.58 eV for c-7.3 at. % F:In−O, and then falls slightly to 2.51 eV for c-9.2 at. % F:In−O. For the amorphous samples, the reverse trend is observed and the band gap
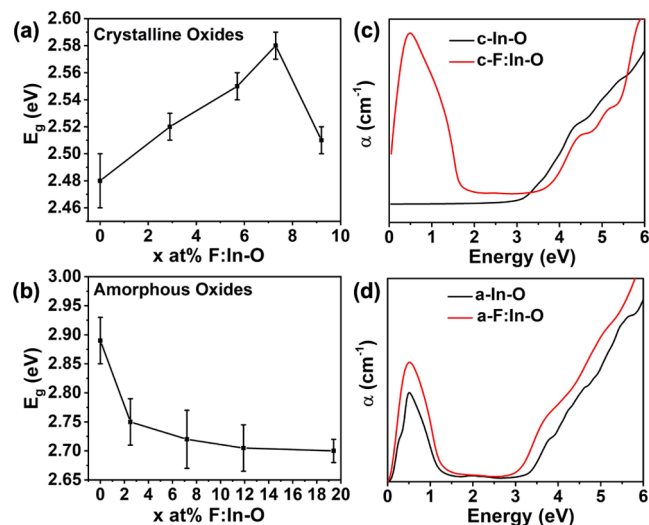

Figure 4. Band gap (E_g) value of indicated (a) crystalline x at. % F:In−O and (b) amorphous x at. % F:In−O. Optical absorption spectra of (c) crystalline and (d) amorphous In−O and F:In−O, derived from DFT calculation.

Figure 3. Ratio of the M−O−M peak area to total peak area (η_{M-O-M}) in XPS O 1s spectra for the indicated crystalline and amorphous x at. % F:In−O materials.

consistently falls from 2.89 eV for a-In−O, to 2.75 eV for a-2.5 at. % F:In−O, to 2.72 eV for a-7.2 at. % F:In−O, to 2.71 eV for a-11.9 at. % F:In−O to 2.7 eV to a-19.4 at. % F:In−O (Table S11 and Figure 4b). This is in excellent agreement with DFT calculations (Figure 4c,d; vide infra). The different trends in the band gaps of F⁻-doped crystalline and amorphous indium oxide arise from different mechanisms of F⁻ incorporation. In bixbyite F:In−O, fluoride appears either as an oxygen substitution (F_O) or resides within the structural vacancy (F_{int}), as discussed in detail below. Because isolated F_{int} is unstable in the presence of the oxygen vacancy (vide infra), F defects that partially compensate oxygen vacancy act as donor defects, leading to a pronounced shift of the Fermi level up into the conduction band, known as the Burstein−Moss (BM) shift, that broadens the optical window.[72] The decrease in the band gap from c-7.3 to c-9.2 at. % F:In−O may be explained by a competing band gap narrowing mechanism involving electron−electron and electron-impurity scattering, in agreement with previous literature reports.[73−75] In contrast, amorphous oxides lack specific symmetry-defined lattice sites, and so, F-substitution on O sites is not possible, whereas interstitial F attains the desired ionic bonding with In because structural reconfiguration is energetically inexpensive in a disordered lattice. As a result, fluoride is not a donor defect in amorphous oxide. At the same time, F⁻-doping increases disorder in the medium and long range structure and affects the coordination morphology in amorphous indium oxide by reducing the number of octahedrally coordinated In polyhedra and hence suppressing the s−s hybridization along the InO_6 chains—in accord with the observed decrease in carrier mobility.[47] The coordination morphology in disordered metal oxides determines the s−s hybridization and hence governs the width of the conduction band.[76] (Note, the location of the conduction band minimum with respect to the valence band maximum is not affected by F incorporation because the In−O distance does not change upon F doping, as shown below by EXAFS measurements and theoretical simulations.) As a result of the narrower conduction band, the density of states in the conduction band increases, leading to a less pronounced BM shift as compared to the undoped a-In−O and hence to a smaller optical band gap.[47]

TEM Analysis. HR-TEM imaging and electron diffraction (ED) were performed to investigate the microstructure and crystallinity of representative F:In−O samples, specifically (1) c-In−O and c-9.2 at. % F:In−O and (2) a-In−O and a-19.4 at. % F:In−O (Figure 5). Note that the HR-TEM imaging and ED data were acquired over multiple areas (5+) of the samples to acquire a representative data set. The insets of Figure 5 show SAED patterns for each sample, depicting sample crystallinity. For the amorphous samples (Figure 5a,b), the SAED patterns show wide diffuse rings, confirming a higher degree of amorphicity of the samples. However, nanocrystalline inclusions can also be observed in the HR-TEM images, which are colored in green and representative areas are circled in red (Figure 5a,b). This suggests that the nanocrystal size is ∼9 nm in the a-In−O sample, while the nanocrystal size decreases to ∼5 nm in the a-19.4 at. % F:In−O sample, indicating that F⁻-doping suppresses crystallization. Interestingly, both samples are macroscopically amorphous (or "X-ray amorphous") as shown by GIXRD (Figure 1b). These observations are in complete agreement with literature data that "X-ray amorphous" In−O can have nanocrystalline inclusions.[77] For the crystalline samples, the SAED patterns
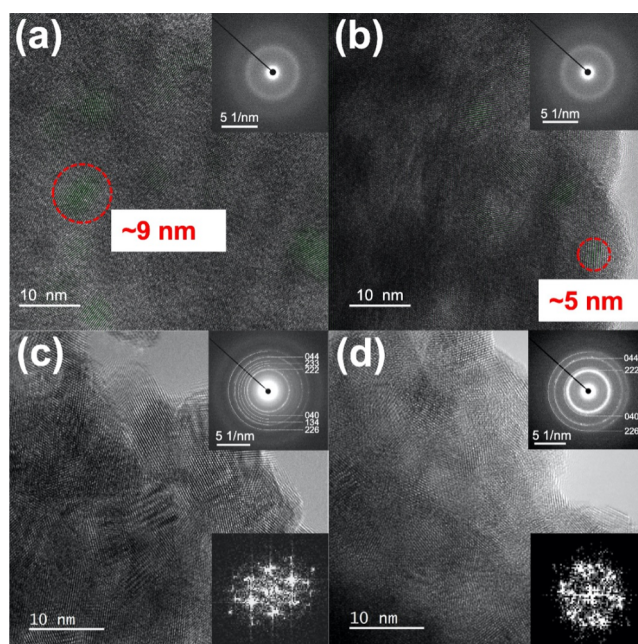

Figure 5. HR-TEM micrographs of amorphous (a) In−O and (b) 19.4 at. % F:In−O; crystalline (c) In−O and (d) 9.2 at. % F:In−O samples with the corresponding SAED patterns as insets. Insets in (c,d) bottom are the representative FFT pattern from one grain from the respective powder.

show sharp rings and atomic columns observable by HR-TEM, which give clear spots in the corresponding fast Fourier transform (FFT) pattern. The SAED patterns of both crystalline samples can be indexed with the In_2O_3 bixbyite structure, but some diffraction rings, such as (134) and (233), are not observed in the c-9.2 at. % F:In−O sample. Compared to c-In−O, c-9.2 at. % F:In−O is less crystallized, which is apparent from the wider and more diffuse rings in the diffraction pattern (Figure 5c,d). Therefore, in all cases, F⁻-doping decreases the crystallinity as evident in the diffuse rings in the diffraction patterns in crystalline oxide and reduction in grain size in amorphous oxide. Thus, the TEM results complement the ¹¹⁵In solid-state NMR data and are in good accord with the EXAFS data and MD simulations (vide infra).

EXAFS Analysis of In−O Versus F:In−O. EXAFS analysis was performed to gain insights into the microstructural changes in the InO_x polyhedral due to fluoride incorporation (Table S12, Figures 6 and S17). Measurements were recorded at the In K-edge (27 940 eV) for two sets of powder samples smeared on quartz: (1) c-In−O and c-9.2 at. % F:In−O and (2) a-In−O and a-19.4 at. % F:In−O. Qualitative EXAFS data analysis included the first three shells for the crystalline samples and the first two shells for the amorphous samples.
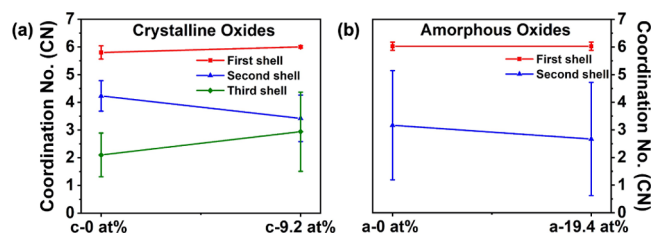

Figure 6. CN of the indicated (a) crystalline and (b) amorphous x at. % F:In−O.

The structure of crystalline In_2O_3 provides the basis for understanding the In−O and F:In−O samples. The In_2O_3 structure consists of In atoms surrounded by octahedra containing six oxygen atoms and two structural vacancies. Two possible arrangements for the structural vacancies allow the octahedra to be in corner- or edge-sharing configurations, leading to the formation of three nearest neighbor shells surrounding the In atom: (1) first shell: In−O with a coordination number (CN) of 6 and average bond distance of 2.18 Å; (2) second shell: In−In with a coordination of 6 and average bond distance of 3.34 Å; and (3) third shell: In−In with a coordination of 6 and average bond distance of 3.83 Å.[77] Increasing disorder in In−O matrices is primarily indicated by decreased CN in the second shell.[33]

For both the undoped and F⁻-doped c-In−O samples, three distinct peaks are present in the pseudo-radial distribution functions (p-RDFs) of the samples, corresponding to the three coordination shells (Figure S17). However, the coordination of the second and third shells in both c-In−O and c-F:In−O is noticeably lower than that for the crystalline In_2O_3 reference (CN = 6) (Table S12).[77] When considering the effect of F⁻-doping on the c-In−O sample, the greatest effect is apparent in the second and third shells, with F⁻-doping having only a minimal effect on the CN and bond distance within the first shell (Table S12). In comparison, the CN of the second shell falls from 4.23 to 3.42 and the average In−In bond distance is decreased from 3.355 to 3.325 Å upon the fluoride addition (Table S12 and Figure 6a). Note that the large error bar in the second and third shell can be explained by relatively weak intensity of the second and third shell scattering and intercorrelation among three variables (CN, bond length, and variance). Although the EXAFS-extracted CNs are within error bars, the mean value of CN decreases with the increasing F⁻ content, in a manner consistent with ^{115}In solid-state NMR (Figure 2c), TEM data (Figure 5), theoretical predictions (vide infra), and literature reports.[33] In the third shell, the trend is reversed, with the coordination increasing from 2.10 to 2.94 and the average bond distance increasing from 3.883 to 3.914 Å.

In the amorphous In−O samples, only a small peak corresponding to the second shell is present, while the third shell is suppressed in the p-RDFs (Figure S17). Again, F⁻-doping seems to have little effect on the first shell, with both the CN and In−O bond distance unchanged by the addition of fluoride (Table S12). The coordination of the second shell shows the same trend as in the crystalline sample, with the CN decreasing from 3.17 to 2.67 with F⁻-doping (Figure 6b). Note that the large error bar in the second shell data can be explained by relatively weak intensity of second shell scattering and the fact that three variables (CN, bond length, and bond variance) are correlated. Although the EXAFS-extracted CNs are within error bars, the mean value of CN decreases with the increasing F⁻ content, in agreement with ^{115}In solid-state NMR (Figure 2d), TEM data (Figure 5), MD calculations (vide infra), and literature report.[33] The In−In bond distance, however, shows little sensitivity to the addition of fluoride and remains the same for the two samples (Table S12).

DFT Calculations on Crystalline F:In−O. Fluoride doping in bixbyite In_2O_3 occurs when F substitutes an oxygen (F_O) or resides in the structural vacancy (F_{int}). An isolated F_O (donor) leads to the formation of four InO_5F with optimized In−F distances of 2.21, 2.29, 2.32, and 2.43 Å. In contrast, an isolated F_{int} in stoichiometric In_2O_3 (acceptor) creates six

InO_6F with identical In−F distances of 2.55 Å in each case. Importantly, our calculations reveal that the formation energy of F_{int} decreases by as much as 4 eV in the presence of a nearby F_O as compared to the oxide without such a defect. The energy gain arises from recombination of the donor electron and the acceptor hole to attain full charge compensation of an oxygen vacancy with two F atoms. To determine the interaction between two F defects in the charge-neutral state, total energy calculations were performed for eight $In_{32}O_{47}F_2$ (6 at. % F) structures with various distances between F_O and F_{int}. The results show that the lowest energy is achieved when this distance is shortest (2.4 Å) and both F_O and F_{int} become neighbors to an In atom, creating InO_5F_2 with elongated distances to two oxygen atoms (Figure 7a). In addition, this
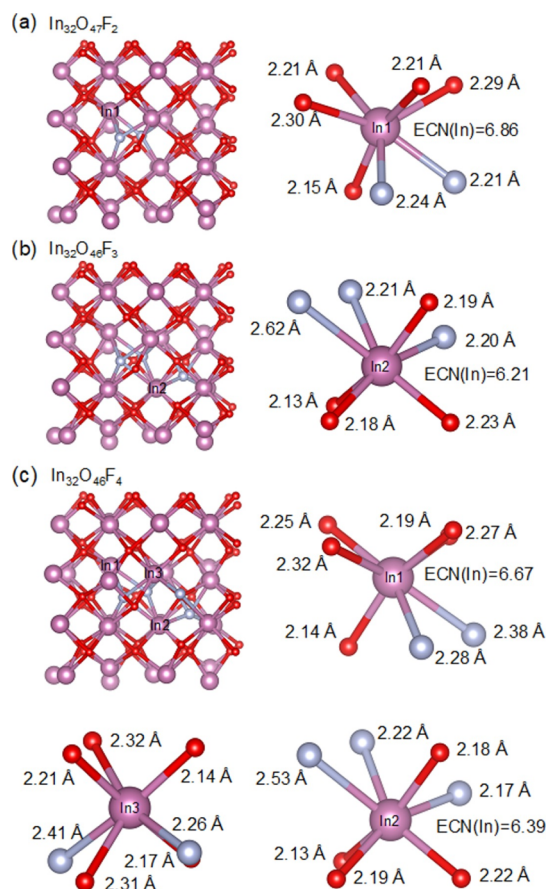

Figure 7. Optimized atomic structure of crystalline F:In−O. (a) Cell of $In_{32}O_{47}F_2$ (6 at. % F) and the structure of InO_5F_2. (b) Cell of $In_{32}O_{46}F_3$ (9 at. % F) and the structure of InO_4F_3. (c) Cell of $In_{32}O_{46}F_4$ (11 at. % F) and the structure of two InO_5F_2 and InO_4F_3.

configuration features three InO_5F and only one In that has F as a seventh neighbor (InO_6F). In structures with longer distances between F_O and F_{int} (3.8 Å or above), the defects can be considered isolated, giving rise to four InO_5F and six InO_6F, respectively, and the total energy is 0.4−0.9 eV higher as compared to that for the case with the shortest F_O−F_{int} distance. These results suggest that F_O and F_{int} attract in crystalline indium oxide, and the driving force for the formation of the F_O−F_{int} complex is the charge recombination and reduction in the number of InO_6F, that is, to minimize the number of In atoms that have single F in the first shell. Accordingly, when F concentration increases, a structure with
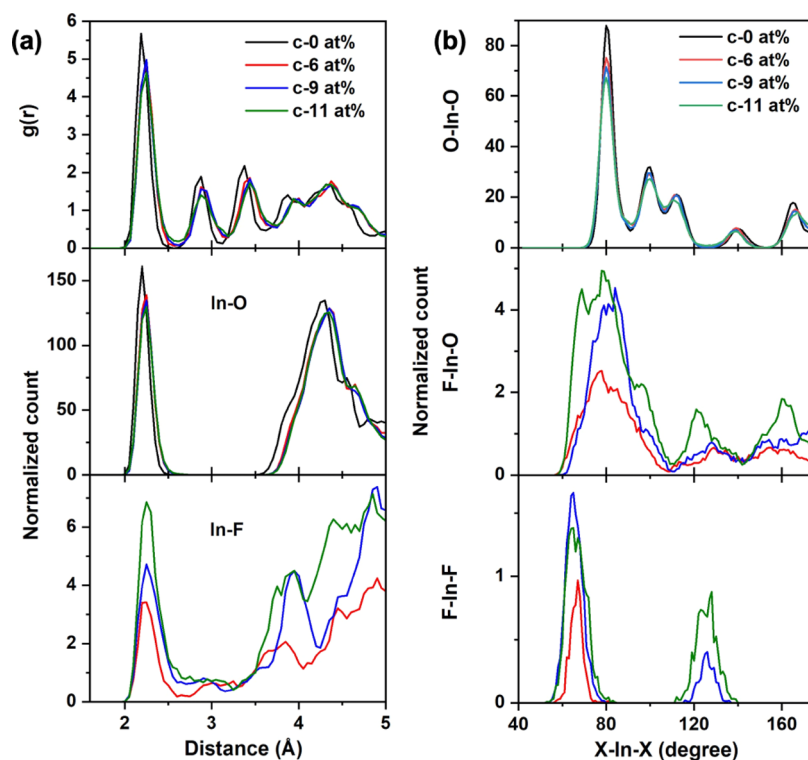
Figure 8. Calculated structural properties of crystalline F:In−O. (a) Pair correlation function and distance distributions for the indicated F concentrations. (b) Anion-resolved angle distributions as a function of F concentration.
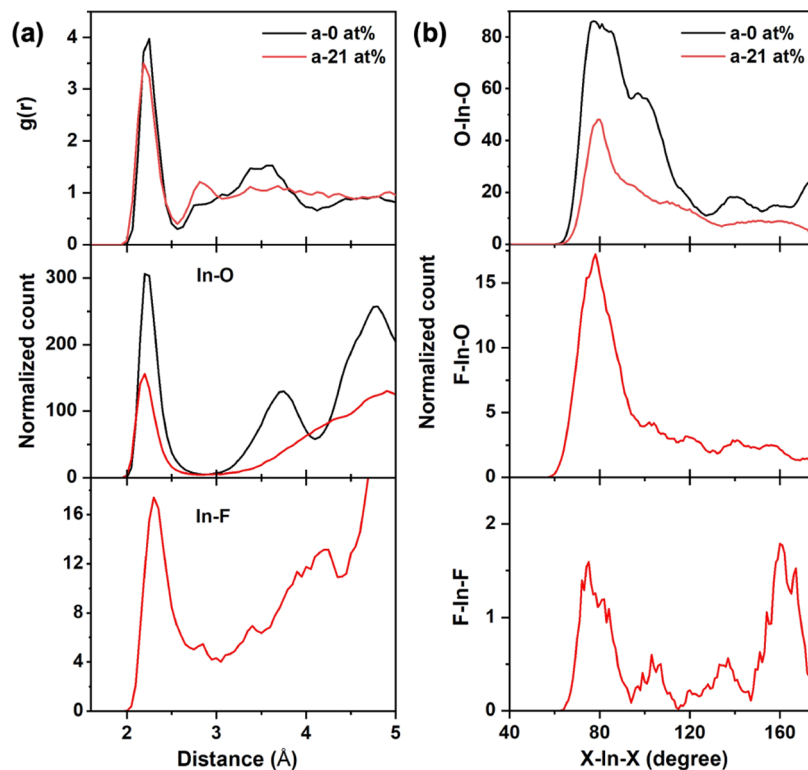

Figure 9. Calculated structural properties of amorphous F:In−O. (a) Pair correlation function and distance distributions for the indicated F concentrations. (b) Anion-resolved angle distributions as a function of F concentration.

InO_3F_3 configuration (Figure 7b) is found to have the lowest total energy among 47 $In_{32}O_{46}F_3$ (9 at. % F) structures with various distances between F_O and the F_O-F_{int} complex. In this case, the two substitutional defects are connected via F_{int} forming a $F_O-F_{int}-F_O$ complex with a long F_O-F_O distance, 4.28 Å. Importantly, configurations with shorter F_O-F_O distances are higher in energy by at least 0.2 eV, suggesting that the F_O defects have weak repulsive interaction when both

belong to the same In atom and prefer large $F_O–In–F_O$ angles, 125°, whereas the two $F_O–In–F_{int}$ angles are two times smaller, 60–68°.

To understand the relative stability of the InO_4F_2 and InO_3F_3 configurations, the F concentration in crystalline indium oxide is increased further by considering $In_{32}O_{46}F_4$ (11 at. % F) structures with seven possible locations for the second F_{int} with respect to the $F_O–F_{int}–F_O$ complex. It is found that formation of a second InO_3F_3, which would occur if the additional interstitial F joined the existing complex to become $F_{int}–F_O–F_{int}–F_O$, is least favorable energetically (+0.24 eV). A formation of higher-F configuration, InO_2F_4, or addition of an isolated F_{int} are also unlikely (+0.12 eV). The most energetically favorable structure is when the second F_{int} forms a new InO_4F_2 with a large $F_O–In–F_{int}$ angle 123° (0 eV, reference energy). Further analysis of the lowest-energy structure reveals that all three InO_4F_2 become unstable and switch to InO_5F with a seventh F atom having the longest distance within the polyhedron (Figure 7c). At the same time, InO_3F_3 shows the opposite trend by pulling two of its F neighbors closer (*c.f.*, Figure 7b,c). Thus, the presence of F_{int} that occupy structural vacancies in bixbyite In_2O_3 and have a tendency to cluster with F_O defects and destabilize InO_4F_2 explains the large fraction of InO_3F_3 found in crystalline samples using ^{19}F MAS NMR analysis (Figure S12).

Fluoride doping in crystalline In_2O_3 and the formation of InO_3F_3 due to $F_O–F_{int}$ clustering have a minimal impact on the first-shell structure as can be seen from the calculated pair correlation function, as well as In–O distance and In–O–In angle distributions as a function of F concentration, Figure 8. However, the presence of longer In–F distances within 2.5–3.0 Å (Figure 8a) and smaller F–In–O and F–In–F angles as compared to O–In–O (Figure 8b) disturb the medium-range structure, that is, the second and third shells, increasing disorder in the lattice. This result is in agreement with the present HR-TEM, EXAFS, and NMR measurements (Table S12). Note that the observed increase in the first-shell CN in F^--doped oxide (from 5.8 for c-0 at. % to 6.0 for c-9.2 at. %, Table S12) is attributed to a small fraction of overcoordinated In (InO_6F and InO_5F_2) associated with isolated or unbound F_{int} defects.

DFT Calculations of Amorphous F:In–O. In marked contrast to the crystalline indium oxide, the amorphous phase lacks symmetry-defined sites and periodicity; therefore, fluoride incorporation is not constrained in the disordered oxide. Moreover, structural rearrangement required to accommodate an impurity in the amorphous phase is energetically inexpensive, so that F attains its desired ionic bonding with In without disturbing the In–O matrix.

Figure 9 presents the calculated pair distribution function as well as distance and angle distributions for amorphous $In_{54}O_{80}$ and $In_{54}O_{73}F_{14}$ (20.6 at. % F). Similar to the crystalline oxide, the presence of F has little effect on the In–O first shell peak, whereas it suppresses the structural features in the medium range, that is, above 2.8 Å, resulting in a more disordered structure as compared to undoped a-In–O. Importantly, the In–F distance distribution between the first and second peaks is significant, suggesting that long In–F distances, 2.5–3.0 Å, are more common than in crystalline F:In–O (Figure 8a). Being at the outer edge of the first shell, these long-distance In–F pairs determine the coordination type of In and are likely to contribute to switching between InO_6 and InO_5F, or InO_5F and InO_4F_2, or InO_4F_2 and InO_3F_3, especially when temper-

ature fluctuations are present. The switching between different coordination types enabled by the wider distribution of In–F distances as compared to that for In–O is likely to be the reason for the much broader ^{115}In NMR spectrum in fluorinated amorphous oxide (Figure 2d), although on average, the first-shell distortions remain similar in a-In–O and a-F:In–O as measured by EXAFS (Table S12).

On comparing the F–In–F and F–In–O angle distributions in the crystalline and amorphous oxides, two important differences are noticed: (i) the first peak in both distributions nearly coincides with that for O–In–O in the disordered oxide. This means that F^- ions maintain the structural characteristics of the In–O polyhedra upon doping of the amorphous structure and do not come close to each other—unlike in F^--doped bixbyite, which features small F–In–F angles of 65° (Figure 8b). (ii) The amorphous oxide has a significant fraction of large F–In–F angles (160°) that were absent in the crystalline case. The large F–In–F angles correspond to two F^- ions being across from each other in a polyhedron. Such a configuration was found to be energetically unfavorable in c-F:In–O.

Thus, the more uniform, symmetry-unrestricted distribution of F in the amorphous structure leads to a larger fraction of InO_4F_2 as compared to InO_3F_3. In DFT-relaxed structure $In_{54}O_{73}F_{14}$ (20.6 at. % F), we account for a 3:2 ratio for the number of InO_4F_2:InO_3F_3 configurations, which is in excellent agreement with the ^{19}F MAS NMR analysis (Figure S13).

CONCLUSIONS

Utilizing solution-based combustion and sol–gel processes, pure F^--doped In–O powders were obtained in crystalline and amorphous forms, respectively. GIXRD and XPS data confirm the microstructure and chemical composition of the synthesized powders. The F 1s binding energies and shifts in the In 3d XPS spectrum reveal that the fluoride ion is ionically bound to In in both crystalline and amorphous F:In–O. UV–vis optical data establish that while the band gap increases with F^--doping in the crystalline oxides, the reverse trend is observed in the amorphous oxides, in excellent agreement with the DFT calculations. Next, the fluoride and In chemical environments were investigated utilizing ^{19}F and ^{115}In solid-state NMR. The ^{19}F MAS NMR reveals that upon fluorination, the InO_3F_3 environment is predominant in crystalline oxides, and the InO_4F_2 environment is predominant in amorphous oxides. From ^{115}In static solid-state NMR, it can be qualitatively concluded that C_Q increases with F^--doping in both crystalline and amorphous F:In–O compared to crystalline and amorphous undoped In–O, indicating increased disorder in the F^--doped system. Supporting this fact are the HR-TEM images, which establish that grain size decreases in amorphous oxides and diffraction pattern gets wider and diffused in crystalline oxide with F^--doping. These results are in close agreement with MD simulation and EXAFS data. Thus, utilizing both experimental and theoretical analyses, it can be concluded that F^- suppresses crystallization in both amorphous and crystalline In–O matrices. This is the first study to establish fluoride as a universal amorphizing agent in the In–O system, and by inference, it may play a similar role in many other oxide materials. These observations also convey significant implications for display and transparent electronics technologies.

■ EXPERIMENTAL SECTION

Crystalline and Amorphous Indium Oxide Sample Synthesis. All reagents were purchased from Sigma-Aldrich and were used without further purification.

Precursor Solution for Crystalline Samples. Exactly 1.7744 g of $In(NO_3)_3 \cdot xH_2O$ was dissolved in 100 mL of 2-methoxyethanol before the addition of 500 μL of acetylacetone and 225 μL of ammonium hydroxide solution (14.5 M), and the resulting 0.05 M solution was stirred for 12−14 h. In separate HDPE vials, adequate amounts of NH_4F were dissolved in Milli-Q water to prepare 0.025, 0.075, 0.15, and 0.25 M solutions. Approximately 1 h prior to spin coating, 2 mL of Milli-Q water/0.025 M/0.075 M/0.15 M/0.25 M NH_4F solution was added to 20 mL of combustion precursor solution along with 70 μL of conc. HNO_3 acid to afford the required F:In ratio.

Precursor Solution for Amorphous Samples. Exactly 1.7744 g of $In(NO_3)_3 \cdot xH_2O$ was dissolved in 100 mL of 2-methoxyethanol and the resulting 0.05 M solution was stirred for 12−14 h. In separate HDPE vials, adequate amounts of NH_4F were dissolved in Milli-Q water to prepare 0.025, 0.075, 0.15, and 0.25 M solutions. Approximately 1 h prior to spin coating, 2 mL of Milli-Q water/ 0.025 M/0.075 M/0.15 M/0.25 M NH_4F solution was added to 20 mL of combustion precursor solution along with 70 μL of conc. HNO_3 acid to afford the required F:In ratio.

F:In−O Powder Synthesis. n^{++}-Si wafers were used as substrates. Before drop-casting, the substrates were cleaned ultrasonically in a 1:1 mixture of isopropyl alcohol and acetone for three times (10 min each), followed by 5 min in an O_2 plasma. Then, precursor solutions were filtered through a 0.2 μm syringe PTFE membrane. Then, 2 mL of filtered solution was drop-cast on the Si wafer and then annealed on a hot plate at 120 °C for 1 min followed by drop-casting 3 mL of the solution on the Si wafer and annealing at 250 °C for 10 min (amorphous oxides)/330 °C for 5 min (crystalline oxides). This process was repeated four times to synthesize ~60 mg amorphous/ crystalline x at. % F:In−O samples.

InOF Synthesis. Powder In_2O_3 (Alfa Aesar, 99.994%) was mixed with NH_4HF_2 (98%, Sigma-Aldrich) in a 1:3.25 weight ratio and ground in a mortar and pestle with acetone as an aid for grinding. The homogenized mixture was put into the capped Al_2O_3 crucible, heated to 420 °C at 5 °C/min (air atmosphere), dwelled for 12 h, and cooled to room temp at 5 °C/min (Figure S18).

Ba₂InO₃F Synthesis. Stoichiometric amounts of $BaCO_3$, BaF_2, and In_2O_3 (Alfa Aesar, 99.994%) were ground together with acetone as a milling aid. The well-mixed powders were transferred to an Al_2O_3 boat and heated to 1050 °C for 12 h in air two times, with intermittent regrinding (Figure S19).

Sample Characterizations. GIXRD measurements were carried out with a Rigaku SmartLab Thin-film Diffraction Workstation using a high intensity 9 kW copper rotating anode X-ray source, which is coupled to a multilayer optic.

Diffuse reflectance UV−vis spectra were acquired using a PerkinElmer LAMBDA 1050 UV−vis−NIR spectrophotometer using drop-casted samples prepared on silicon substrates. The acquired diffuse reflectance spectrum is converted to the Kubelka− Munk function $F(R_\infty)$ using eq 1[71]

$$F(R_\infty) = \frac{(1 - R_\infty)^2}{2R_\infty} \tag{1}$$

where R_∞ is the reflectance of an infinitely thick specimen. Putting $F(R_\infty)$ instead of α (absorption coefficient) into the Tauc method yields eq 2[71]

$$(F(R_\infty) \cdot h\nu)^{1/n} = B(h\nu - E_g) \tag{2}$$

where h is the Planck constant, ν is the photon's frequency, E_g is the band gap energy, and B is a constant. The n factor depends on the nature of the electronic transition.

XPS analyses were performed with a Thermo Scientific ESCALAB 250Xi at a base pressure of 4.5×10^{-10} mbar. Spectra were obtained after the surface of the film was etched for about ~720 s to minimize

surface contamination. HR-TEM images and SAED patterns were obtained using a JEOL Grand ARM 300F operated at 300 kV. The In−O and F:In−O powders were cleaved from the substrate and dropped on ultrathin carbon-coated Cu grids as TEM samples.

NMR experiments were performed at the National High Magnetic Field Laboratory (NHMFL). ^{19}F and ^{1}H experiments were performed on a Bruker Avance-III 500 (11.8 T) spectrometer using a 2.5 mm Bruker probe with a sample spinning rate of 25 kHz for ^{19}F measurements and 20 kHz for ^{1}H of all F:In−O samples. ^{19}F spectra were obtained using a rotor-synchronized spin-echo pulse with a $\pi/2$ pulse length of 4.4 μs and a recycle delay of 50 s. The chemical shift of ^{19}F NMR spectra was calibrated with LiF at δ −201 ppm. ^{1}H NMR spectra were collected using a rotor-synchronized spin-echo pulse with a $\pi/2$ pulse length of 1.8 μs and recycle delay of 20 s. The resonance was calibrated using adamantane at δ 1.84 ppm. ^{115}In static solid-state, NMR experiments were conducted on an 830 MHz (19.6 T) spectrometer at a Larmor frequency of 181.875 MHz. The spectra were acquired using a $\pi/5$ pulse of 1.5 μs with a recycle delay of 0.1 s. The spectra of crystalline and amorphous samples were acquired using a stepping frequency in increments of ±166 kHz with the QCPMG pulse sequence. For Ba_2InO_3F only: ^{19}F CPMAS data were recorded on a 400 MHz Bruker Avance III HD NMR spectrometer with a Phoenix NMR 1.6 mm HFX probe at an ambient temperature of about 23 °C. The Hahn echo pulse sequence was used. The spinning rate was set at 38 kHz. The ^{19}F Larmor frequency was 376.087 MHz. The ^{19}F NMR shifts were referenced to an external $NaPF_6$ peak at δ −82.5 ppm.

EXAFS measurements were performed at beamline 5BM-D at the Advanced Photon Source at Argonne National Laboratory. Data were collected at the In k-edge (27940 eV). Powder samples of crystalline and amorphous InO and F:InO [(1) c-In−O and c-9.2 at. % F:In−O and (2) a-In−O and a-19.4 at. % F:In−O] were uniformly spread on tape and measured in transmission mode. Crystalline In_2O_3 powder was used as a reference. The normalized linear EXAFS absorption coefficient $\chi(k)$ was fit using eq 3

$$\chi(k) = \sum_i \frac{S_0^2 N_i f_i(k)}{kR_i^2} \sin[2kR_i + \delta(k)] e^{-2R_i/\lambda(k)} e^{-2k^2\sigma_{R_i}^2} \tag{3}$$

where S_0^2 is the intrinsic loss factor, $\lambda(k)$ is the electron mean free path, N_i and R_i are the CN and bond distance of the ith shell of the absorbing atom, $f_i(k)$ and $\delta(k)$ are the backscattering amplitude and the phase shift, and $e^{-2k^2\sigma_{R_i}^2}$ is the Debye−Waller factor—a measure of the structural disorder or variation in R_i. The Fourier transform of $\chi(k)$ generates a p-RDF for the absorbing atom, which is fit to extract how the CN, bond distances, and Debye−Waller factors vary as a function of fluoride doping. Data reduction and analysis were performed using the Demeter software package.[78] The initial model was obtained by using FEFF simulations based on crystalline In_2O_3. The intrinsic loss factor ($S_0^2 = 1.013$) was determined from the fit to the crystalline reference sample. Fittings were carried out over the R-range 1.0−4.0 Å. A k-weight of 2 was used for all fitting. Data in the k-range of 2.4−14.65 Å^{-1} were used for the crystalline samples and 2.4− 12 Å^{-1} for the amorphous samples.

Theoretical Analysis. Crystalline and amorphous indium oxide structures with and without F$^-$-doping were calculated using Vienna Ab initio Simulation Package (VASP).[79−82] The calculations are based on DFT[83,84] with periodic boundary conditions and use PBE functional[85,86] within the projector augmented-wave method.[87,88] In crystalline cases, a bixbyite In_2O_3 structure with 80-atom cell was employed. Two, three, or four F atoms were added to the structure as substitutional and/or interstitial defects and the oxygen stoichiometry was adjusted accordingly. The total energy calculations were performed for the fully relaxed structures for all possible respective locations of the F defects in the lattice. For the optimization, a cut-off energy of 500 eV and the $4 \times 4 \times 4$ Γ-centered k-point were used; the atomic positions were relaxed until the Hellmann−Feynman force on each atom was below 0.01 eV/Å. The electronic and optical properties of the optimized amorphous In-based oxides were

calculated using the hybrid Heyd−Scuseria−Ernzerhof (HSE06) approach[89,90] with a mixing parameter of 0.25 and a screening parameter α of 0.2 Å^{-1}. Optical absorption was derived from the frequency-dependent dielectric function, $\varepsilon(\omega) = \varepsilon_1(\omega) + i\varepsilon_2(\omega)$, calculated within independent particle approximation in VASP. The imaginary part, $\varepsilon_2(\omega)$, is related to the optical absorption at a given frequency, ω, and is determined based on the electronic transitions of the hybrid functional solution. The real part of the complex dielectric function is obtained using Kramers−Kronig relations. The resulting atomic structures were plotted using VESTA software.[91]

To obtain amorphous structures, we employed an *ab initio* MD liquid-quench approach as implemented in VASP. A bixbyite cell of In_2O_3 with a crystalline density of 7.12 g/cm^3 and with 134 atoms per cell was used as the initial structure, which was melted at 3000 K to eliminate any crystalline memory. For F:In−O with 20.6 at. % F, fluoride atoms were randomly introduced into the cell and the number of oxygen atoms was adjusted ($In_{54}O_{73}F_{14}$) to maintain the same anion charge as in undoped indium oxide. To determine the cell density, four different melt-quench cycles were performed for the density values ranging from 6.3 to 6.9 g/cm^3. Based on the total energy calculations, the optimal density was set to 6.7 g/cm^3, which was calculated based on the corresponding fraction of InF_3 having the crystalline density of 4.7 g/cm^3. All structures had additional melting at 3000 K for 10 ps to randomize the multicomponent configuration and stabilize the total energy. Next, liquid quench simulations were performed as follows. Each structure was cooled to 2500 K at the MD rate of 100 K/ps and then rapidly quenched to 100 K at 200 K/ps rate. An energy cut-off of 260 eV and single Γ-point were used during melting and quenching processes. Finally, each structure was equilibrated at 300 K for 6 ps with a cut-off energy of 400 eV. All MD simulations were carried out in the NVT ensemble with the Nose−Hoover thermostat using an integration time step of 2 fs. For an accurate structural analysis of the simulated amorphous oxides (pair correlation function as well as distance and angle distributions), the room-temperature In−O and F:In−O structures were used. The atomic configurations obtained from the *ab initio* MD simulations were optimized within DFT using the PBE functional to analyze the In-[O,F] coordination.

■ ASSOCIATED CONTENT

Ⓢ Supporting Information

The Supporting Information is available free of charge at https://pubs.acs.org/doi/10.1021/acs.chemmater.2c00053.

Supporting Information is available free of charge on the ACS Publications website. XPS, solid-state NMR data, UV−vis data, EXAFS data, and so forth (PDF)

■ AUTHOR INFORMATION

Corresponding Authors

Kenneth R. Poeppelmeier − *Department of Chemistry and the Materials Research Center, Northwestern University, Evanston, Illinois 60208, United States*; Email: krp@northwestern.edu

Vinayak P. Dravid − *Department of Materials Science and Engineering, and the Materials Research Center and The NUANCE Center, Northwestern University, Evanston, Illinois 60208, United States*; ⓞ orcid.org/0000-0002-6007-3063; Email: v-dravid@northwestern.edu

Michael J. Bedzyk − *Department of Materials Science and Engineering, and the Materials Research Center, Northwestern University, Evanston, Illinois 60208, United States*; ⓞ orcid.org/0000-0002-1026-4558; Email: bedzyk@northwestern.edu

Julia E. Medvedeva − *Department of Physics, Missouri University of Science and Technology, Rolla, Missouri 65409,*

United States; ⓞ orcid.org/0000-0001-7142-1644; Email: juliaem@mst.edu

Yan-Yan Hu − *Department of Chemistry and Biochemistry, Florida State University, Tallahassee, Florida 32306, United States*; ⓞ orcid.org/0000-0003-0677-5897; Email: yhu@fsu.edu

Antonio Facchetti − *Department of Chemistry and the Materials Research Center, Northwestern University, Evanston, Illinois 60208, United States; Flexterra Inc., Skokie, Illinois 60077, United States*; ⓞ orcid.org/0000-0002-8175-7958; Email: a-facchetti@northwestern.edu

Tobin J. Marks − *Department of Chemistry and the Materials Research Center, Northwestern University, Evanston, Illinois 60208, United States*; ⓞ orcid.org/0000-0001-8771-0141; Email: t-marks@northwestern.edu

Authors

Aritra Sil − *Department of Chemistry and the Materials Research Center, Northwestern University, Evanston, Illinois 60208, United States*

Michael J. Deck − *Department of Chemistry and Biochemistry, Florida State University, Tallahassee, Florida 32306, United States*; ⓞ orcid.org/0000-0001-6439-8634

Elise A. Goldfine − *Department of Materials Science and Engineering, and the Materials Research Center, Northwestern University, Evanston, Illinois 60208, United States*

Chi Zhang − *Department of Materials Science and Engineering, and the Materials Research Center, Northwestern University, Evanston, Illinois 60208, United States*; ⓞ orcid.org/0000-0002-6116-5437

Sawankumar V. Patel − *Department of Chemistry and Biochemistry, Florida State University, Tallahassee, Florida 32306, United States*; ⓞ orcid.org/0000-0002-5293-9330

Steven Flynn − *Department of Chemistry and the Materials Research Center, Northwestern University, Evanston, Illinois 60208, United States*; ⓞ orcid.org/0000-0001-8262-6987

Haoyu Liu − *Department of Chemistry and Biochemistry, Florida State University, Tallahassee, Florida 32306, United States*

Po-Hsiu Chien − *Department of Chemistry and Biochemistry, Florida State University, Tallahassee, Florida 32306, United States*; ⓞ orcid.org/0000-0002-1607-1271

Complete contact information is available at:
https://pubs.acs.org/10.1021/acs.chemmater.2c00053

Author Contributions

¶A.S. and M.D. contributed equally.

Notes

The authors declare no competing financial interest.

■ ACKNOWLEDGMENTS

■ REFERENCES

(1) Park, J. W.; Kang, B. H.; Kim, H. J. A Review of Low-Temperature Solution-Processed Metal Oxide Thin-Film Transistors for Flexible Electronics. *Adv. Funct. Mater.* **2019**, *30*, 1904632.

(2) Xu, W.; Li, H.; Xu, J.-B.; Wang, L. Recent Advances of Solution-Processed Metal Oxide Thin-Film Transistors. *ACS Appl. Mater. Interfaces* **2018**, *10*, 25878.

(3) Carlos, E.; Leppäniemi, J.; Sneck, A.; Alastalo, A.; Deuermeier, J.; Branquinho, R.; Martins, R.; Fortunato, E. Printed, Highly Stable Metal Oxide Thin-Film Transistors with Ultra-Thin High-K Oxide Dielectric. *Adv. Electron. Mater.* **2020**, *6*, 1901071.

(4) Chen, R.; Lan, L. Solution-Processed Metal-Oxide Thin-Film Transistors: A Review of Recent Developments. *Nanotechnology* **2019**, *30*, 312001.

(5) Nomura, K.; Ohta, H.; Takagi, A.; Kamiya, T.; Hirano, M.; Hosono, H. Room-Temperature Fabrication of Transparent Flexible Thin-Film Transistors Using Amorphous Oxide Semiconductors. *Nature* **2004**, *432*, 488.

(6) Lee, M.; Jo, J. W.; Kim, Y. J.; Choi, S.; Kwon, S. M.; Jeon, S. P.; Facchetti, A.; Kim, Y. H.; Park, S. K. Corrugated Heterojunction Metal-Oxide Thin-Film Transistors with High Electron Mobility Via Vertical Interface Manipulation. *Adv. Mater.* **2018**, *30*, 1804120.

(7) Jeong, J. K. The Status and Perspectives of Metal Oxide Thin-Film Transistors for Active Matrix Flexible Displays. *Semicond. Sci. Technol.* **2011**, *26*, 034008.

(8) Labram, J. G.; Lin, Y.-H.; Zhao, K.; Li, R.; Thomas, S. R.; Semple, J.; Androulidaki, M.; Sygellou, L.; McLachlan, M.; Stratakis, E.; Amassian, A.; Anthopoulos, T. D. Signatures of Quantized Energy States in Solution-Processed Ultrathin Layers of Metal-Oxide Semiconductors and Their Devices. *Adv. Funct. Mater.* **2015**, *25*, 1727.

(9) Yeon Kwon, J.; Kyeong Jeong, J. Recent Progress in High Performance and Reliable N-Type Transition Metal Oxide-Based Thin Film Transistors. *Semicond. Sci. Technol.* **2015**, *30*, 024002.

(10) Thomas, S. R.; Pattanasattayavong, P.; Anthopoulos, T. D. Solution-Processable Metal Oxide Semiconductors for Thin-Film Transistor Applications. *Chem. Soc. Rev.* **2013**, *42*, 6910.

(11) Yu, X.; Marks, T. J.; Facchetti, A. Metal Oxides for Optoelectronic Applications. *Nat. Mater.* **2016**, *15*, 383.

(12) Fortunato, E.; Barquinha, P.; Martins, R. Oxide Semiconductor Thin-Film Transistors: A Review of Recent Advances. *Adv. Mater.* **2012**, *24*, 2945.

(13) Kim, H. J.; Park, K.; Kim, H. J. High-Performance Vacuum-Processed Metal Oxide Thin-Film Transistors: A Review of Recent Developments. *J. Soc. Inf. Disp.* **2020**, *28*, 591.

(14) Ide, K.; Nomura, K.; Hosono, H.; Kamiya, T. Electronic Defects in Amorphous Oxide Semiconductors: A Review. *Phys. Status Solidi A* **2019**, *216*, 1800372.

(15) Kumar, B.; Kaushik, B. K.; Negi, Y. S. Perspectives and Challenges for Organic Thin Film Transistors: Materials, Devices, Processes and Applications. *J. Mater. Sci.: Mater. Electron.* **2013**, *25*, 1.

(16) Paterson, A. F.; Singh, S.; Fallon, K. J.; Hodsden, T.; Han, Y.; Schroeder, B. C.; Bronstein, H.; Heeney, M.; McCulloch, I.; Anthopoulos, T. D. Recent Progress in High-Mobility Organic Transistors: A Reality Check. *Adv. Mater.* **2018**, *30*, No. e1801079.

(17) Wang, C.; Zhang, X.; Dong, H.; Chen, X.; Hu, W. Challenges and Emerging Opportunities in High-Mobility and Low-Energy-Consumption Organic Field-Effect Transistors. *Adv. Energy Mater.* **2020**, *10*, 2000955.

(18) Divya Bharathi, N.; Sivasankaran, K. Research Progress and Challenges of Two Dimensional Mos2 Field Effect Transistors. *J. Semiconduct.* **2018**, *39*, 104002.

(19) Liu, Y.; Duan, X.; Shin, H.-J.; Park, S.; Huang, Y.; Duan, X. Promises and Prospects of Two-Dimensional Transistors. *Nature* **2021**, *591*, 43.

(20) Zhou, N.; Kim, M.-G.; Loser, S.; Smith, J.; Yoshida, H.; Guo, X.; Song, C.; Jin, H.; Chen, Z.; Yoon, S. M.; Freeman, A. J.; Chang, R. P. H.; Facchetti, A.; Marks, T. J. Amorphous Oxide Alloys as Interfacial Layers with Broadly Tunable Electronic Structures for Organic Photovoltaic Cells. *Proc. Natl. Acad. Sci. U.S.A.* **2015**, *112*, 7897.

(21) Jaisutti, R.; Kim, J.; Park, S. K.; Kim, Y.-H. Low-Temperature Photochemically Activated Amorphous Indium-Gallium-Zinc Oxide for Highly Stable Room-Temperature Gas Sensors. *ACS Appl. Mater. Interfaces* **2016**, *8*, 20192.

(22) Wang, B.; Thukral, A.; Xie, Z.; Liu, L.; Zhang, X.; Huang, W.; Yu, X.; Yu, C.; Marks, T. J.; Facchetti, A. Flexible and Stretchable Metal Oxide Nanofiber Networks for Multimodal and Monolithically Integrated Wearable Electronics. *Nat. Commun.* **2020**, *11*, 2405.

(23) Huang, F.; Kim, S. Y.; Rao, Z.; Lee, S.-J.; Yoon, J.; Park, J. H.; Hong, W.-K. Protein Biophotosensitizer-Based Igzo Photo-Thin Film Transistors for Monitoring Harmful Ultraviolet Light. *ACS Appl. Bio Mater.* **2019**, *2*, 3030.

(24) Hennek, J. W.; Smith, J.; Yan, A.; Kim, M.-G.; Zhao, W.; Dravid, V. P.; Facchetti, A.; Marks, T. J. Oxygen ″Getter″ Effects on Microstructure and Carrier Transport in Low Temperature Combustion-Processed a-Inxzno (X = Ga, Sc, Y, La) Transistors. *J. Am. Chem. Soc.* **2013**, *135*, 10729.

(25) Choi, Y.; Kim, G. H.; Jeong, W. H.; Bae, J. H.; Kim, H. J.; Hong, J.-M.; Yu, J.-W. Carrier-Suppressing Effect of Scandium in Inzno Systems for Solution-Processed Thin Film Transistors. *Appl. Phys. Lett.* **2010**, *97*, 162102.

(26) Qadri, S. B.; Kim, H. Synthesis of Bulk In2o3−Sc2o3 and Their Transparent Conducting Oxide Films. *J. Appl. Phys.* **2002**, *92*, 227.

(27) Shin, H. S.; Kim, G. H.; Jeong, W. H.; Ahn, B. D.; Kim, H. J. Electrical Properties of Yttrium−Indium−Zinc-Oxide Thin Film Transistors Fabricated Using the Sol−Gel Process and Various Yttrium Compositions. *Jpn. J. Appl. Phys.* **2010**, *49*, 03CB01.

(28) Paine, D. C.; Yaglioglu, B.; Beiley, Z.; Lee, S. Amorphous Izo-Based Transparent Thin Film Transistors. *Thin Solid Films* **2008**, *516*, 5894.

(29) Moffitt, S. L.; Zhu, Q.; Ma, Q.; Falduto, A. F.; Buchholz, D. B.; Chang, R. P. H.; Mason, T. O.; Medvedeva, J. E.; Marks, T. J.; Bedzyk, M. J. Probing the Unique Role of Gallium in Amorphous Oxide Semiconductors through Structure−Property Relationships. *Adv. Electron. Mater.* **2017**, *3*, 1700189.

(30) Huang, W.; Chien, P.-H.; McMillen, K.; Patel, S.; Tedesco, J.; Zeng, L.; Mukherjee, S.; Wang, B.; Chen, Y.; Wang, G.; Wang, Y.; Gao, Y.; Bedzyk, M. J.; DeLongchamp, D. M.; Hu, Y.-Y.; Medvedeva, J. E.; Marks, T. J.; Facchetti, A. Experimental and Theoretical Evidence for Hydrogen Doping in Polymer Solution-Processed Indium Gallium Oxide. *Proc. Natl. Acad. Sci. U.S.A.* **2020**, *117*, 18231.

(31) Huang, W.; Guo, P.; Zeng, L.; Li, R.; Wang, B.; Wang, G.; Zhang, X.; Chang, R. P. H.; Yu, J.; Bedzyk, M. J.; Marks, T. J.; Facchetti, A. Metal Composition and Polyethylenimine Doping Capacity Effects on Semiconducting Metal Oxide-Polymer Blend Charge Transport. *J. Am. Chem. Soc.* **2018**, *140*, 5457.

(32) Huang, W.; Zeng, L.; Yu, X.; Guo, P.; Wang, B.; Ma, Q.; Chang, R. P. H.; Yu, J.; Bedzyk, M. J.; Marks, T. J.; Facchetti, A. Metal Oxide Transistors Via Polyethylenimine Doping of the Channel Layer: Interplay of Doping, Microstructure, and Charge Transport. *Adv. Funct. Mater.* **2016**, *26*, 6179.

(33) Yu, X.; Zeng, L.; Zhou, N.; Guo, P.; Shi, F.; Buchholz, D. B.; Ma, Q.; Yu, J.; Dravid, V. P.; Chang, R. P. H.; Bedzyk, M.; Marks, T. J.; Facchetti, A. Ultra-Flexible, "Invisible" Thin-Film Transistors Enabled by Amorphous Metal Oxide/Polymer Channel Layer Blends. *Adv. Mater.* **2015**, *27*, 2390.

(34) Chen, Y.; Huang, W.; Sangwan, V. K.; Wang, B.; Zeng, L.; Wang, G.; Huang, Y.; Lu, Z.; Bedzyk, M. J.; Hersam, M. C.; Marks, T. J.; Facchetti, A. Polymer Doping Enables a Two-Dimensional Electron Gas for High-Performance Homojunction Oxide Thin-Film Transistors. *Adv. Mater.* **2019**, *31*, 1805082.

(35) Mori, T.; Kajihara, K.; Kanamura, K.; Toda, Y.; Hiramatsu, H.; Hosono, H. Indium-Based Ultraviolet-Transparent Electroconductive Oxyfluoride Inof: Ambient-Pressure Synthesis and Unique Electronic Properties in Comparison with In2o3. *J. Am. Chem. Soc.* **2013**, *135*, 13080.

(36) Harada, J. K.; Charles, N.; Poeppelmeier, K. R.; Rondinelli, J. M. Heteroanionic Materials by Design: Progress toward Targeted Properties. *Adv. Mater.* **2019**, *31*, No. e1805295.

(37) Kageyama, H.; Hayashi, K.; Maeda, K.; Attfield, J. P.; Hiroi, Z.; Rondinelli, J. M.; Poeppelmeier, K. R. Expanding Frontiers in Materials Chemistry and Physics with Multiple Anions. *Nat. Commun.* **2018**, *9*, 772.

(38) Shannon, R. D. Revised Effective Ionic Radii and Systematic Studies of Interatomic Distances in Halides and Chalcogenides. *Acta Crystallogr., Sect. A: Cryst. Phys., Diffr., Theor. Gen. Crystallogr.* **1976**, *32*, 751.

(39) Wang, D.; Jiang, J.; Furuta, M. Investigation of Carrier Generation Mechanism in Fluorine-Doped N+-in−Ga−Zn-O for Self-Aligned Thin-Film Transistors. *J. Disp. Technol.* **2016**, *12*, 258.

(40) Qian, L. X.; Tang, W. M.; Lai, P. T. Improved Characteristics of Ingazno Thin-Film Transistor by Using Fluorine Implant. *ECS Solid State Lett.* **2014**, *3*, P87.

(41) Jiang, J.; Toda, T.; Hung, M. P.; Wang, D.; Furuta, M. Highly Stable Fluorine-Passivated in−Ga−Zn−O Thin-Film Transistors under Positive Gate Bias and Temperature Stress. *Appl. Phys. Express* **2014**, *7*, 114103.

(42) Qian, L. X.; Lai, P. T. Fluorinated Ingazno Thin-Film Transistor with Hflao Gate Dielectric. *IEEE Electron Device Lett.* **2014**, *35*, 363.

(43) Rahaman, A.; Billah, M. M.; Um, J. G.; Hasan, M. M.; Jang, J. Effect of Doping Fluorine in Offset Region on Performance of Coplanar a-Igzo Tfts. *IEEE Electron Device Lett.* **2018**, *39*, 1318.

(44) Seo, J.-S.; Jeon, J.-H.; Hwang, Y. H.; Park, H.; Ryu, M.; Park, S.-H. K.; Bae, B.-S. Solution-Processed Flexible Fluorine-Doped Indium Zinc Oxide Thin-Film Transistors Fabricated on Plastic Film at Low Temperature. *Sci. Rep.* **2013**, *3*, 2085.

(45) Chang, J.; Lin, Z.; Lin, M.; Zhu, C.; Zhang, J.; Wu, J. Solution Processed F Doped Zno (Zno:F) for Thin Film Transistors and Improved Stability through Co-Doping with Alkali Metals. *J. Mater. Chem. C* **2015**, *3*, 1787.

(46) Jeon, J.-H.; Hwang, Y. H.; Jin, J.; Bae, B.-S. Low-Temperature Aqueous Solution Processed Fluorine-Doped Zinc Tin Oxide Thin-Film Transistors. *MRS Commun.* **2012**, *2*, 17.

(47) Sil, A.; Avazpour, L.; Goldfine, E. A.; Ma, Q.; Huang, W.; Wang, B.; Bedzyk, M. J.; Medvedeva, J. E.; Facchetti, A.; Marks, T. J. Structure−Charge Transport Relationships in Fluoride-Doped Amorphous Semiconducting Indium Oxide: Combined Experimental and Theoretical Analysis. *Chem. Mater.* **2019**, *32*, 805.

(48) Ye, Z.; Wong, M. Characteristics of Thin-Film Transistors Fabricated on Fluorinated Zinc Oxide. *IEEE Electron Device Lett.* **2012**, *33*, 549.

(49) Xu, W.; Cao, H.; Liang, L.; Xu, J.-B. Aqueous Solution-Deposited Gallium Oxide Dielectric for Low-Temperature, Low-Operating-Voltage Indium Oxide Thin-Film Transistors: A Facile

Route to Green Oxide Electronics. *ACS Appl. Mater. Interfaces* **2015**, *7*, 14720.

(50) Noh, H.-K.; Chang, K. J.; Ryu, B.; Lee, W.-J. Electronic Structure of Oxygen-Vacancy Defects in Amorphous in-Ga-Zn-O Semiconductors. *Phys. Rev. B: Condens. Matter Mater. Phys.* **2011**, *84*, 115205.

(51) Medvedeva, J. E.; Khanal, R. Long-Range Structural Correlations in Amorphous Ternary in-Based Oxides. *Vacuum* **2015**, *114*, 142.

(52) King, P. D. C.; Veal, T. D.; Fuchs, F.; Wang, C. Y.; Payne, D. J.; Bourlange, A.; Zhang, H.; Bell, G. R.; Cimalla, V.; Ambacher, O.; Egdell, R. G.; Bechstedt, F.; McConville, C. F. Band Gap, Electronic Structure, and Surface Electron Accumulation of Cubic and Rhombohedralin2o3. *Phys. Rev. B: Condens. Matter Mater. Phys.* **2009**, *79*, 205211.

(53) Fuchs, F.; Bechstedt, F. Indium-Oxide Polymorphs from First Principles: Quasiparticle Electronic States. *Phys. Rev. B: Condens. Matter Mater. Phys.* **2008**, *77*, 155107.

(54) Kim, M.-G.; Kanatzidis, M. G.; Facchetti, A.; Marks, T. J. Low-Temperature Fabrication of High-Performance Metal Oxide Thin-Film Electronics Via Combustion Processing. *Nat. Mater.* **2011**, *10*, 382.

(55) Moulder, J. F.; Chastain, J. *Handbook of X-Ray Photoelectron Spectroscopy: A Reference Book of Standard Spectra for Identification and Interpretation of XPS Data*; Physical Electronics Division Perkin-Elmer Corp., 1992.

(56) Scholz, G.; Kemnitz, E. Mechanochemical Synthesis of Alf3 with Nh4f as Fluorinating Agent − Does It Work? *Solid State Sci.* **2009**, *11*, 676.

(57) Zheng, A.; Liu, S.-B.; Deng, F. 19f Chemical Shift of Crystalline Metal Fluorides: Theoretical Predictions Based on Periodic Structure Models. *J. Phys. Chem. C* **2009**, *113*, 15018.

(58) Chupas, P. J.; Corbin, D. R.; Rao, V. N. M.; Hanson, J. C.; Grey, C. P. A Combined Solid-State Nmr and Diffraction Study of the Structures and Acidity of Fluorinated Aluminas: Implications for Catalysis. *J. Phys. Chem. B* **2003**, *107*, 8327.

(59) Ashbrook, S. E. Recent Advances in Solid-State Nmr Spectroscopy of Quadrupolar Nuclei. *Phys. Chem. Chem. Phys.* **2009**, *11*, 6892.

(60) Hamaed, H.; Johnston, K. E.; Cooper, B. F. T.; Terskikh, V. V.; Ye, E.; Macdonald, C. L. B.; Arnold, D. C.; Schurko, R. W. A115in Solid-State Nmr Study of Low Oxidation-State Indium Complexes. *Chem. Sci.* **2014**, *5*, 982.

(61) Griffith, K. J.; Ding, F.; Flynn, S. Solid-State Nuclear Magnetic Resonance of Spin-9/2 Nuclei (115) in and (209) Bi in Functional Inorganic Complex Oxides. *Magn. Reson. Chem.* **2021**, *59*, 1077.

(62) O'Dell, L. A.; Schurko, R. W. Qcpmg Using Adiabatic Pulses for Faster Acquisition of Ultra-Wideline Nmr Spectra. *Chem. Phys. Lett.* **2008**, *464*, 97.

(63) Chen, K. A Practical Review of NMR Lineshapes for Spin-1/2 and Quadrupolar Nuclei in Disordered Materials. *Int. J. Mol. Sci.* **2020**, *21*, 5666.

(64) Madsen, R. S. K.; Qiao, A.; Sen, J.; Hung, I.; Chen, K.; Gan, Z.; Sen, S.; Yue, Y. Ultrahigh-Field (67)Zn Nmr Reveals Short-Range Disorder in Zeolitic Imidazolate Framework Glasses. *Science* **2020**, *367*, 1473.

(65) Wasylishen, R. E.; Ashbrook, S. E.; Wimperis, S. *NMR of Quadrupolar Nuclei in Solid Materials*; John Wiley & Sons, 2012.

(66) Donley, C.; Dunphy, D.; Paine, D.; Carter, C.; Nebesny, K.; Lee, P.; Alloway, D.; Armstrong, N. R. Characterization of Indium−Tin Oxide Interfaces Using X-Ray Photoelectron Spectroscopy and Redox Processes of a Chemisorbed Probe Molecule: Effect of Surface Pretreatment Conditions. *Langmuir* **2001**, *18*, 450.

(67) Kamiya, T.; Nomura, K.; Hirano, M.; Hosono, H. Electronic Structure of Oxygen Deficient Amorphous Oxide Semiconductor a-Ingazno4-X: Optical Analyses and First-Principle Calculations. *Phys. Status Solidi C* **2008**, *5*, 3098.

(68) Nomura, K.; Kamiya, T.; Hirano, M.; Hosono, H. Origins of Threshold Voltage Shifts in Room-Temperature Deposited and

Annealed a-in—Ga—Zn—O Thin-Film Transistors. *Appl. Phys. Lett.* **2009**, *95*, 013502.

(69) Wang, B.; Zeng, L.; Huang, W.; Melkonyan, F. S.; Sheets, W. C.; Chi, L.; Bedzyk, M. J.; Marks, T. J.; Facchetti, A. Carbohydrate-Assisted Combustion Synthesis to Realize High-Performance Oxide Transistors. *J. Am. Chem. Soc.* **2016**, *138*, 7067.

(70) Chen, Y.; Wang, B.; Huang, W.; Zhang, X.; Wang, G.; Leonardi, M. J.; Huang, Y.; Lu, Z.; Marks, T. J.; Facchetti, A. Nitroacetylacetone as a Cofuel for the Combustion Synthesis of High-Performance Indium—Gallium—Zinc Oxide Transistors. *Chem. Mater.* **2018**, *30*, 3323.

(71) Mishra, V.; Warshi, M. K.; Sati, A.; Kumar, A.; Mishra, V.; Sagdeo, A.; Kumar, R.; Sagdeo, P. R. Diffuse Reflectance Spectroscopy: An Effective Tool to Probe the Defect States in Wide Band Gap Semiconducting Materials. *Mater. Sci. Semicond. Process.* **2018**, *86*, 151.

(72) Medvedeva, J. E. Magnetically Mediated Transparent Conductors: In2o3 Doped with Mo. *Phys. Rev. Lett.* **2006**, *97*, 086401.

(73) Gupta, L.; Mansingh, A.; Srivastava, P. K. Band Gap Narrowing and the Band Structure of Tin-Doped Indium Oxide Films. *Thin Solid Films* **1989**, *176*, 33.

(74) Saw, K. G.; Mishra, Y. K.; Aznan, N. M.; Yam, F. K.; Ng, S. S.; Pung, S. Y. New Insights on the Burstein-Moss Shift and Band Gap Narrowing in Indium-Doped Zinc Oxide Thin Films. *PLoS One* **2015**, *10*, No. e0141180.

(75) Sanon, G.; Rup, R.; Mansingh, A. Band-Gap Narrowing and Band Structure in Degenerate Tin Oxide (Sno2) Films. *Phys. Rev. B: Condens. Matter Mater. Phys.* **1991**, *44*, 5672.

(76) Medvedeva, J. E.; Buchholz, D. B.; Chang, R. P. H. Recent Advances in Understanding the Structure and Properties of Amorphous Oxide Semiconductors. *Adv. Electron. Mater.* **2017**, *3*, 1700082.

(77) Buchholz, D. B.; Ma, Q.; Alducin, D.; Ponce, A.; Jose-Yacaman, M.; Khanal, R.; Medvedeva, J. E.; Chang, R. P. H. The Structure and Properties of Amorphous Indium Oxide. *Chem. Mater.* **2014**, *26*, 5401.

(78) Ravel, B.; Newville, M. Athena, Artemis, Hephaestus: Data Analysis for X-Ray Absorption Spectroscopy Usingifeffit. *J. Synchrotron Radiat.* **2005**, *12*, 537.

(79) Kresse, G.; Hafner, J. Ab Initiomolecular Dynamics for Liquid Metals. *Phys. Rev. B: Condens. Matter Mater. Phys.* **1993**, *47*, 558.

(80) Kresse, G.; Hafner, J. Ab Initio Molecular-Dynamics Simulation of the Liquid-Metal-Amorphous-Semiconductor Transition in Germanium. *Phys. Rev. B: Condens. Matter Mater. Phys.* **1994**, *49*, 14251.

(81) Kresse, G.; Furthmüller, J. Efficiency of Ab-Initio Total Energy Calculations for Metals and Semiconductors Using a Plane-Wave Basis Set. *Comput. Mater. Sci.* **1996**, *6*, 15.

(82) Kresse, G.; Furthmüller, J. Efficient Iterative Schemes for Ab Initiototal-Energy Calculations Using a Plane-Wave Basis Set. *Phys. Rev. B: Condens. Matter Mater. Phys.* **1996**, *54*, 11169.

(83) Hohenberg, P.; Kohn, W. Inhomogeneous Electron Gas. *Phys. Rev.* **1964**, *136*, B864.

(84) Kohn, W.; Sham, L. J. Self-Consistent Equations Including Exchange and Correlation Effects. *Phys. Rev.* **1965**, *140*, A1133.

(85) Perdew, J. P.; Burke, K.; Ernzerhof, M. Generalized Gradient Approximation Made Simple. *Phys. Rev. Lett.* **1996**, *77*, 3865.

(86) Perdew, J. P.; Burke, K.; Ernzerhof, M. Generalized Gradient Approximation Made Simple. *Phys. Rev. Lett.* **1997**, *78*, 1396.

(87) Blöchl, P. E. Projector Augmented-Wave Method. *Phys. Rev. B: Condens. Matter Mater. Phys.* **1994**, *50*, 17953.

(88) Kresse, G.; Joubert, D. From Ultrasoft Pseudopotentials to the Projector Augmented-Wave Method. *Phys. Rev. B: Condens. Matter Mater. Phys.* **1999**, *59*, 1758.

(89) Heyd, J.; Peralta, J. E.; Scuseria, G. E.; Martin, R. L. Energy Band Gaps and Lattice Parameters Evaluated with the Heyd-Scuseria-Ernzerhof Screened Hybrid Functional. *J. Chem. Phys.* **2005**, *123*, 174101.

(90) Heyd, J.; Scuseria, G. E.; Ernzerhof, M. Hybrid Functionals Based on a Screened Coulomb Potential. *J. Chem. Phys.* **2003**, *118*, 8207.

(91) Momma, K.; Izumi, F. Vesta 3for Three-Dimensional Visualization of Crystal, Volumetric and Morphology Data. *J. Appl. Crystallogr.* **2011**, *44*, 1272.